Journal of Materials Chemistry C

ROYAL SOCIETY OF CHEMISTRY

COMMUNICATION

View Article Online
View Journal

Cite this: DOI: 10.1039/d0tc01839b

Received 14th April 2020,
Accepted 20th May 2020

DOI: 10.1039/d0tc01839b

rsc.li/materials-c

Femtosecond laser direct writing of perovskite patterns with whispering gallery mode lasing†

Xiaoyu Tian,[a] Yalun Xu,[b] Hongming Zhao,[c] Xiubo Qin,[c] Yangtian Nie,[a] Wei Li,[b] Sheng Liu,[a] Qianqian Lin *[b] and Qiang Cao*[a]

Hybrid perovskites have recently attracted attention in both materials science and opto-electronics research, because of their excellent opto-electronic properties and facile fabrication. Perovskite-based photovoltaic devices, photodetectors, and light-emitting diodes have exhibited unprecedented success. Moreover, optically pumped perovskite lasers have been reported with various crystal shapes. However, most of these lasers are fabricated from solution-grown micro/nano crystals, and thus lack reproducibility. Here, we present controllable fabrication of formamidinium lead iodide ($FAPbI_3$) perovskite microdisks by thermal co-evaporation, coupled with femtosecond laser direct writing. After careful investigation of dimensional effects, including the impact of diameter and thickness, we achieved an ultra-low threshold of $\sim 3\ \mu J\ cm^{-2}$. Furthermore, we investigated the relationship of lasing performance with carrier dynamics by transient absorption. We found that a longer carrier lifetime can reduce the pump threshold. These microdisk lasers based on femtosecond laser fabrication of evaporated perovskite thin films show exceptional reproducibility, rendering them extremely suitable for mass production; hence, they offer a promising method for low-cost, on-chip coherent light sources.

1. Introduction

Hybrid perovskite microlasers have emerged as promising candidates for high-performance lasing with a low threshold at room temperature;[1–5] they exhibit extraordinary optoelectronic properties, such as a high absorption coefficient,[6] modest charge-carrier lifetime and mobility,[7] a tunable exciton binding energy,[8] and long diffusion lengths.[9] In addition, hybrid perovskites can be prepared *via* low-cost fabrication techniques.[10] Realisation of hybrid perovskite-based microlasers benefits from their unique shape after fabrication. Based on different limiting mechanisms, microcavities can be roughly divided into Fabry–Perot microcavities, photonic crystal microcavities, whispering-gallery-mode (WGM) microcavities, and deformed microcavities.[11–14] In particular, WGM resonators are excellent candidates for development of a semiconductor laser because of their high quality (Q) factor and small volume (V);[15–18] the large Q/V ratio allows for strong coupling between the gain medium and the cavity field, enabling realisation of a low threshold and narrow linewidth laser. Because hybrid perovskites possess a larger refractive index than air and most substrates (glass or quartz), light can easily be trapped within the circular cavity through multiple total reflections. Simultaneously, the light continues to propagate within the cavity, resulting in stable phase coherent enhancement of travelling wave modes and sufficient optical gain.[19]

Fabrication methods for perovskite-based lasers can be divided into two categories: bottom-up and top-down.[20] Bottom-up fabrication methods are dependent on the properties of the crystalline materials themselves; the manufacturing process serves to control the growth parameters of the crystal (*e.g.*, time, temperature, humidity, pressure, and concentration) to form a specific size and shape of microcavity structure. For instance, Liu *et al.* fabricated $MAPbI_3$ perovskite microplate arrays on a silicon substrate with a pre-patterned single-layer hexagonal boron nitride (h-BN) film as the template layer.[21] Feng *et al.* demonstrated a "liquid knife" technique for fabrication of perovskite single-crystalline arrays by using a silicon micropillar template.[22] Wang *et al.* reported a wafer-scale growth method for regular arrays of perovskite microplate crystals.[23] However, the microlasers obtained using these methods are strongly influenced by fabrication conditions; hence, reproducibility is lacking. Compared with bottom-up methods, top-down fabrication techniques have advantages such as large-area fabrication and high controllability. For example, Alias *et al.* used a focused ion beam technique to fabricate binary and circular subwavelength gratings.[24] Xing *et al.* reported a vapor

[a] The Institute of Technological Sciences, Wuhan University, Wuhan 430072, China. E-mail: caoqiang@whu.edu.cn
[b] School of Physics and Technology, Wuhan University, Wuhan 430072, China. E-mail: q.lin@whu.edu.cn
[c] X Lab, the Second Academy of CASIC, Beijing 100854, China

† Electronic supplementary information (ESI) available. See DOI: 10.1039/d0tc01839b

phase synthesis strategy to achieve large-area light-emission.[25] To improve reproducibility and control the lasing wavelength, Zhang *et al.* patterned single crystalline perovskite microplates for $MAPbBr_3$ microdisk lasers through a typical electron beam lithography method and inductively coupled plasma etching.[26] Hörantner *et al.* demonstrated a colloidal monolayer lithography method for control of perovskite crystal domain size and microstructure to obtain a highly ordered metal oxide honeycomb structure.[27] However, lead halide perovskite materials are extremely sensitive to electron beam, water, and polar organic solvents, and are unable to withstand high temperatures (>180 °C); these properties may lead to damage in perovskite samples and deterioration of opto-electronic properties. Hence, lithography or electron beam lithography methods have limited application to perovskites, compared with conventional inorganic semiconductors.[28,29] More recently, thermal nanoimprinting has emerged as a facile and promising technique for fabrication of photonic structures. Pourdavoud *et al.* fabricated patterned perovskite thin films *via* thermal nanoimprinting and achieved perovskite lasers with low threshold and narrow linewidth.[30–32] However, thermal nanoimprinting requires precise design and fabrication of stamps; the process also requires moderate pressure and heating. To the best of our knowledge, there is no facile and effective approach for fabrication of reproducible perovskite microcavities; the development of a reliable mass-production method for lead halide perovskite lasers is essential.

In this work, we produced high-performance microdisk formamidinium lead iodide ($FAPbI_3$) perovskite lasers by femtosecond (fs) laser direct writing. High-quality, large-area perovskite films were prepared by thermal co-evaporation. Fs laser direct writing, as a high-precision method that causes less damage to perovskite materials, achieved ultra-high reliability and reproducibility in processing the evaporated lead halide perovskite thin films with various patterns. Perovskite microdisks with various diameters and thicknesses were also fabricated, and the influence of microdisk dimensions on lasing performance (*e.g.*, threshold) was evaluated.

2. Method

2.1 Preparation of $FAPbI_3$ films

Compared with $MAPbI_3$, $FAPbI_3$-based perovskites have emerged as a more promising composition because of their improved thermal stability and enhanced optoelectronic properties, including a broader absorption spectrum up to ~850 nm in the near-infrared region, a longer carrier lifetime, and fewer trap states.[33,34] Conventionally, $FAPbI_3$ perovskites are obtained *via* spin-coating of precursors, either by single-step deposition of formamidinium

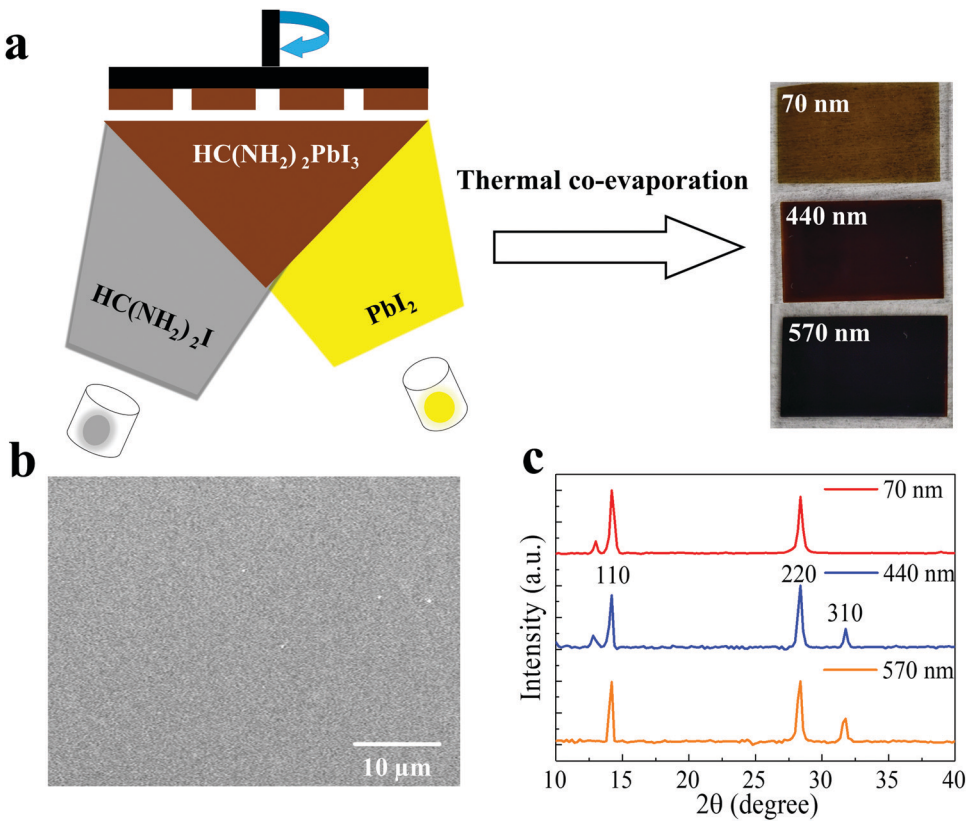

Fig. 1 Preparation of perovskite films. (a) Schematic illustration of thermal co-evaporation (left) and photographs of $FAPbI_3$ thin films prepared with various thickness (right), (b) scanning electron microscopy image of perovskite thin films deposited by co-evaporation, and (c) X-ray diffraction patterns of perovskite films.

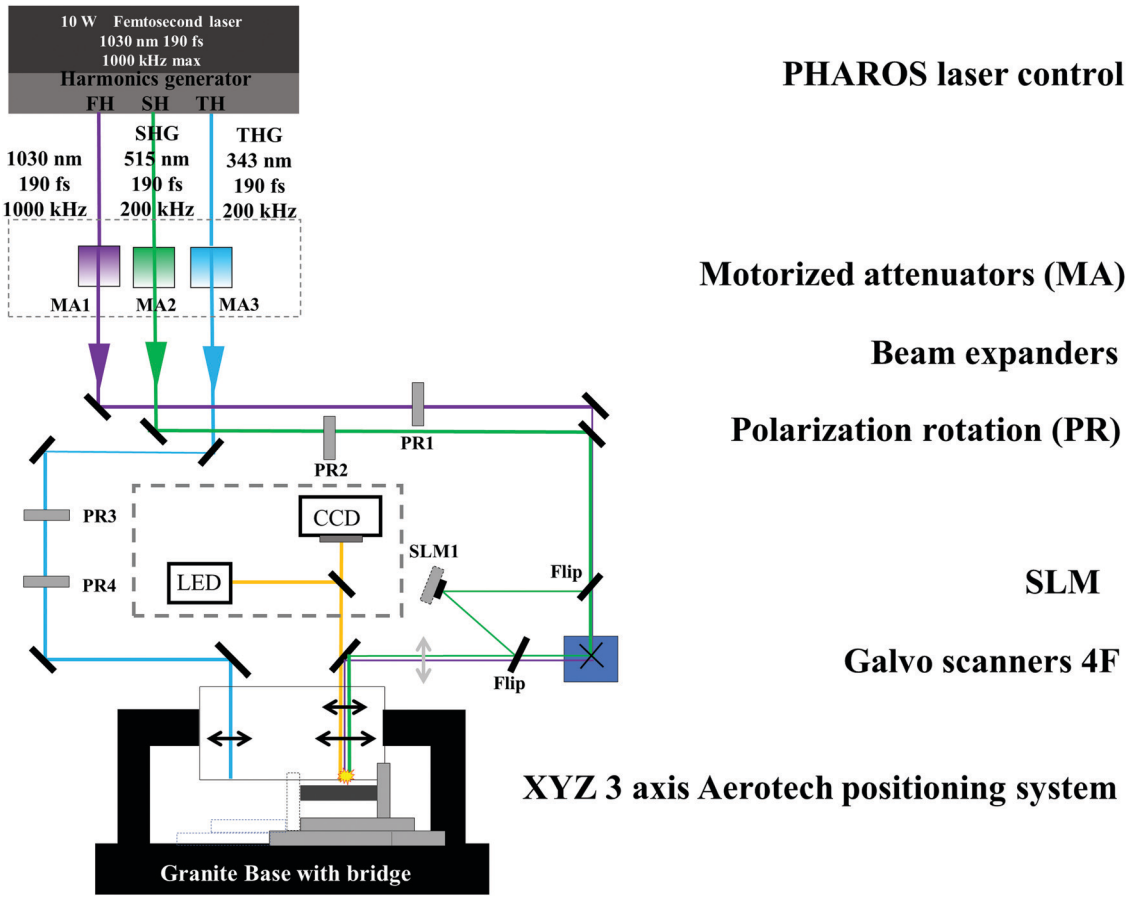

Fig. 2 Schematic of optical setup for perovskite microdisk fabrication.

iodide (FAI) and lead iodide (PbI_2) mixed solution or sequential deposition of FAI and PbI_2 precursors. However, the precursor approach leads to formation of films with poor morphology and an unstable crystal structure that can readily crystallise into two distinct polymorphs: the undesirable photoinactive "yellow" δ-phase (δ-$FAPbI_3$) and the desired photoactive "black" α-phase (α-$FAPbI_3$).[35,36]

In this work, we used thermal co-evaporation to deposit pure α-$FAPbI_3$ films. Fig. 1a illustrates the co-evaporation process (left) and the resulting $FAPbI_3$ thin films with different thicknesses (right) schematically (for fabrication details, see ESI,† S1). As shown in Fig. 1b, perovskite thin films prepared by this method exhibit a uniform and compact microstructure with small grain sizes. For comparison, we also conducted high-resolution atomic force microscopy measurements of the evaporated and spin-coated perovskite films, as shown in Fig. S1 (ESI†). The evaporated films are more uniform with a smaller grain size; they have a root mean square surface roughness (R_q) of 4.56 nm. Fig. 1c shows X-ray diffraction patterns of evaporated perovskite films with thicknesses of 70 nm, 440 nm, and 570 nm. All samples exhibited strong diffraction peaks of the (110) and (220) planes of the perovskite crystal structure at approximately 14° and 28°, respectively. There was also a small peak at approximately 12° belonging to the PbI_2 crystals, which indicated a slight excess of PbI_2 in the thin film samples. Compared with spin-coated perovskite films, these samples exhibited fewer pin-holes and a more uniform surface.[10] The diminished surface roughness can effectively reduce light scattering and provide a better platform for nano/micro patterning, as discussed in the following section.

2.2 Laser writing of $FAPbI_3$ microdisks

To fabricate $FAPbI_3$ microdisk perovskite lasers, we used a fs laser to write directly on perovskite films deposited on quartz substrates. The fabrication process with high pulse energy is complicated, because the laser-induced thermal effect can easily damage the boundary; notably, it can even ruin the perovskite crystals. Hence, the fabrication process is optimised by using a laser power below the single-pulse ablation threshold (optimisation details are provided in ESI,† S2). Perovskite microdisk lasers are fabricated using direct ablation with second-harmonic (515 nm) 190 fs laser pulses from a regenerative amplified Yb:KGW-based laser system (Pharos, Light Conversion). The laser is focused with a microscope objective (50×, NA = 0.42), yielding an in focal-plane diameter of the laser facula of approximately 1–2 μm. Perovskite films were mounted onto a PC-driven nano positioning system (ANT-PLUS series) providing a movement accuracy of <0.25 μm along all three axes. A schematic of the optical setup is shown in Fig. 2.

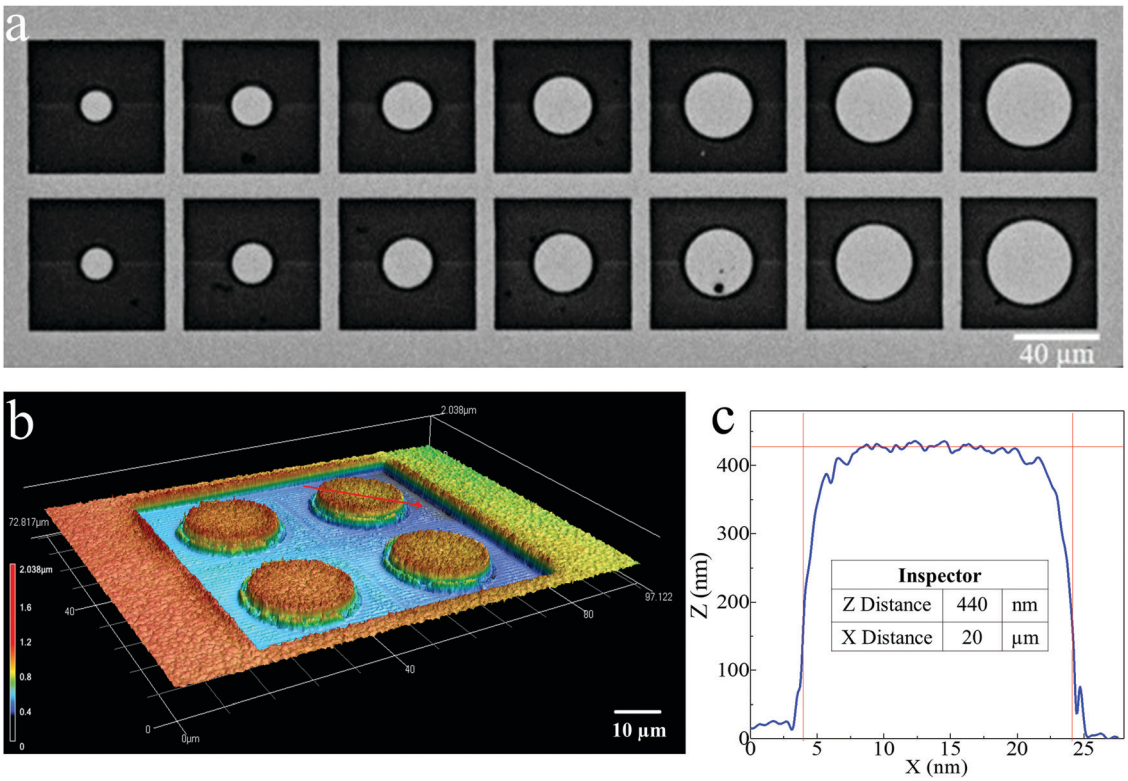

Fig. 3 (a) Scanning electron microscopy image of $FAPbI_3$ microdisks with diameters ranging from 16 to 40 μm and thickness of 440 nm, (b) three-dimensional laser scanning confocal microscope images, and (c) cross-sectional profile of single 440 nm-thick perovskite microdisk with diameter of 20 μm.

To avoid the influence of adjacent microdisks, we removed the surrounding perovskite to produce a 60 × 60 μm^2 lattice. Fig. 3a shows a scanning electron microscopy image of the microdisks, with diameters ranging from 16 to 40 μm (thickness of 440 nm). As shown in Fig. 3a, we observed minimal visible damage around the microdisks; moreover, all microdisks could form an isolated structure. We also performed high-resolution three-dimensional laser scanning using a confocal microscope (VK-1100, KEYENCE), and measured the cross-sectional images of the edges, as shown in Fig. 3b. Fig. 3c shows the cross-sectional profile of a single 440 nm-thick perovskite microdisk with a diameter of 20 μm; relatively smooth and steep edges are present, which demonstrates the high precision of the fs laser direct writing.

3. Results and discussion

3.1 Lasing performance characterisation of samples with different diameters

Individual microdisks were tested using a photoluminescence (PL) system to identify cavity performance for lasing (experimental details and schemes, see ESI,† S3). To ensure uniform energy injection, the spot size of the laser beam was focused to be ~54 μm; this was calibrated with a sharp blade mounted on a microstage moving with a precisely controlled stepper motor. The beam profile (shown in Fig. S4, ESI†) was recorded with a calibrated power meter and fitted with a Gaussian equation. The spot size was sufficiently large to cover the entire cavity, thus ensuring high pumping injection efficiency and reducing the local heating effect. During the experiment, the focal length (50× microscope objective) was slightly adjusted to ensure full coverage of the perovskite microdisk within the laser beam, as shown in the inset of Fig. S4 (ESI†), recorded with a CCD camera. Fig. 4a shows the power-dependent emission spectra of typical $FAPbI_3$ microdisks (thickness ~70 nm; diameter length ~16 μm). When the pump intensity is low, only a broad peak is present at 798 nm. With increasing excitation power, the PL intensity increases slowly. When the pump intensity reaches P_{th} = 3.4 μJ cm^{-2}, a series of periodic peaks emerge and the full width at half maximum value rapidly decreases to approximately 1.88 nm. We plotted one emission peak intensity (marked with *) *versus* pump fluence; clear thresholds (P_{th}) can be extracted (inset of Fig. 4a).

Mode spacing ($\Delta\lambda$) is an important parameter for a typical WGM microcavity. To form a stable oscillation in the cavity, the phase change of the reciprocating light in the perovskite cavity must be an integral multiple of 2π, as follows:[37]

$$nL = 2\pi Rn = m\lambda, \quad (1)$$

where n is the effective refractive index of the micro resonator, L is the round-trip distance in the perovskite cavity, R is the radius of the microdisk, λ is the resonance wavelength, and m is the mode order (integer). Mode spacing ($\Delta\lambda$) between adjacent

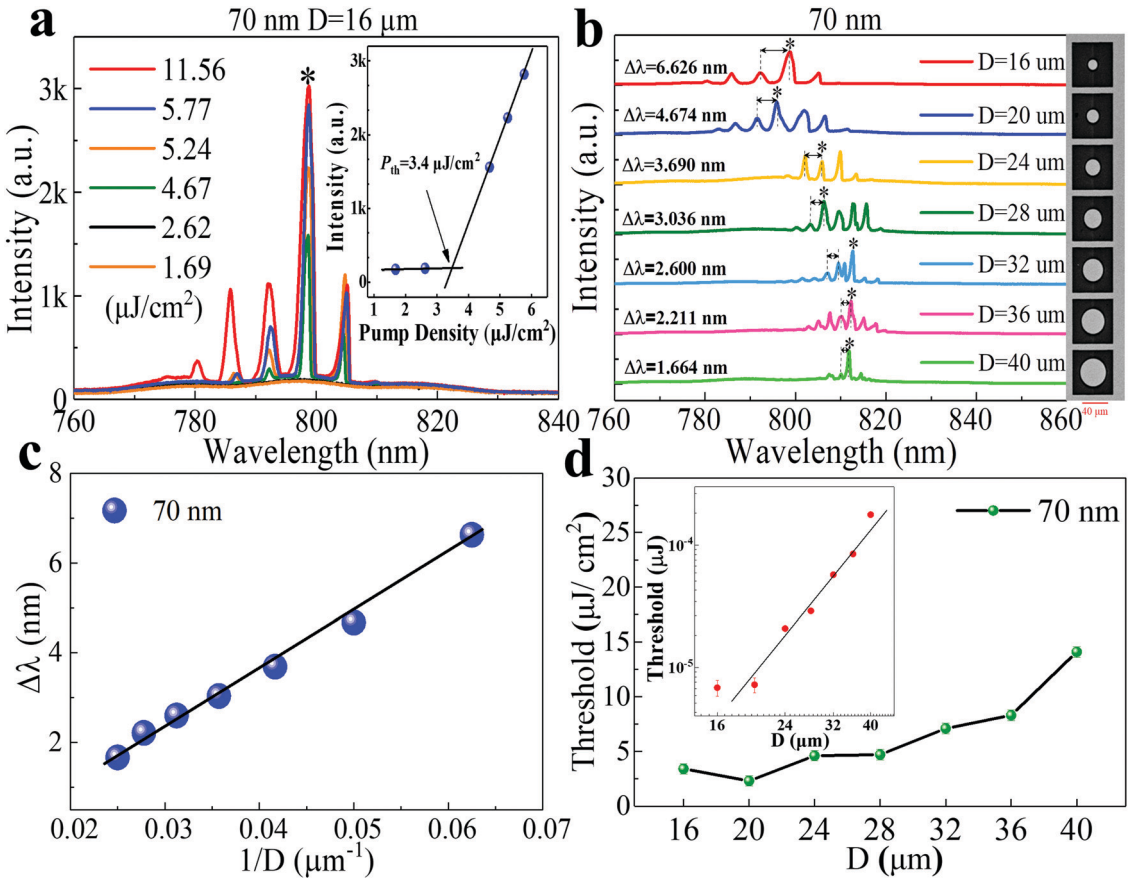

Fig. 4 Lasing performance of 70 nm-thick perovskite microdisks. (a) PL spectra of 70 nm $FAPbI_3$ microdisk with diameter of 16 μm at different intensities. Inset: PL intensity as a function of pump intensity. (b) Emission spectra of perovskite microdisks with different diameters from 16 μm to 40 μm. (c) Mode spacing as a function of 1/*D*. (d) Threshold of pump density as a function of *D*. Inset: Threshold of pump energy as a function of *D*.

laser modes can be expressed as follows:[38]

$$\Delta\lambda = \frac{\lambda^2}{2\pi Rn} \quad (2)$$

From the above equations, the free spectrum range of microdisk lasers can be derived; it is highly dependent on the microdisk radius. To further explore the WGM phenomenon, we used the method in Section 2 to generate various diameters from 20 μm to 40 μm, then test their lasing performance. Microdisks with different diameters have clear lasing peaks with increasing power density, as shown in Fig. S6 (ESI†). Fig. 4b shows the emission spectra of perovskite microdisks with different diameters from 16 μm to 40 μm at the pump intensity above the threshold; notably, each microdisk has a unique lasing mode. In addition, as the diameter increases, the mode spacing ($\Delta\lambda$) becomes smaller and the peak becomes sharper. To further understand the WGM modes in our experiments, we investigated the influence of the microdisk dimensions on lasing performance (*i.e.*, mode spacing and pump threshold).

Fig. 4c shows a linear dependence of mode spacing ($\Delta\lambda$) *versus* cavity size. Microdisks with larger diameter have smaller mode spacing and more modes. Fig. 4d and the inset of Fig. S6 (ESI†) show the threshold of pump density *versus* diameter. More interestingly, the threshold of pump energy clearly increases with increasing disk diameter (shown in the inset of Fig. 4d), indicating that smaller microdisks require a smaller pump threshold for these WGM lasers. Furthermore, the lowest lasing threshold reaches 2.3 μJ cm^{-2}. The observed linear dependence of the lasing threshold on microdisk size is consistent with the cavity-quantum electrodynamics theory.[39,40] This dependence could also be highly influenced by charge carrier trapping and surface states. In contrast, Liu *et al.* observed a reduction in the pump fluence threshold with increasing diameter; this was attributed to the diminished surface-to-volume ratio (*i.e.*, fewer surface states for a single crystal).[21,41] However, our samples were thermal co-evaporated, and the grain size was much smaller than the film thickness and the diameter. Hence, the trapping states may have been located on the surface and homogenously distributed in the bulk, resulting in different behaviours in terms of the diameter dependent threshold.

3.2 Lasing performance characterisation of samples with different thicknesses

To investigate the thickness-dependent lasing properties of $FAPbI_3$ microdisk lasers, we fabricated five microdisks with

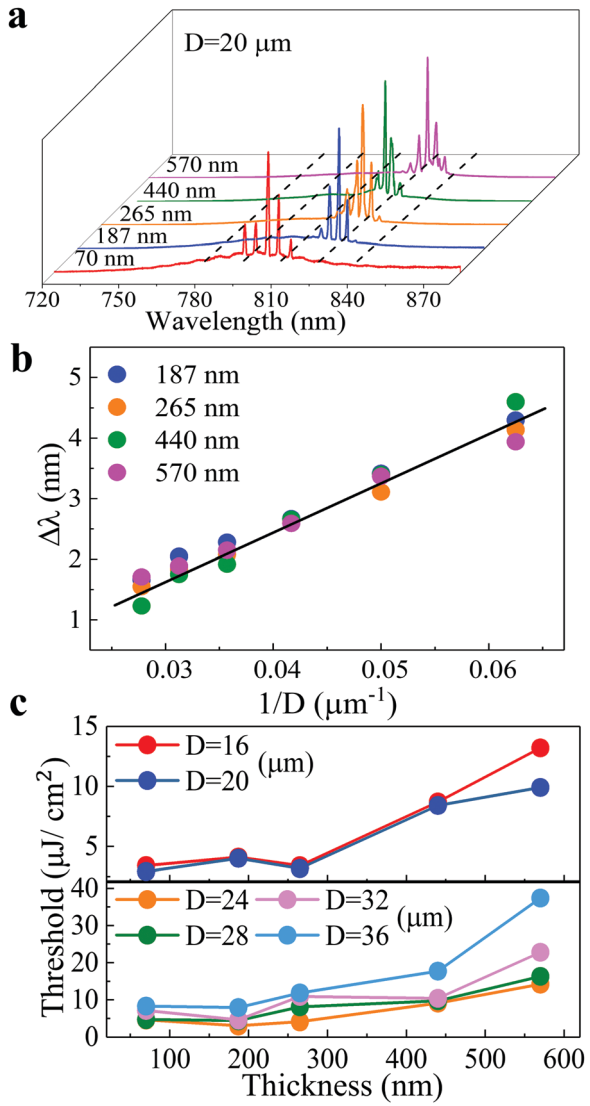

Fig. 5 Thickness-dependent lasing properties (a) emission spectra of perovskite microdisks (20 μm) with various thicknesses, (b) linear dependence of mode spacing *versus* 1/*D*, and (c) lasing threshold of pump density *versus* thickness of microdisks.

identical diameter (20 μm) and various thicknesses. Fig. 5a shows the emission spectra of these samples. Notably, these microdisks exhibited almost nearly identical features with five main WGMs; they also exhibited a slight red shift, induced by band-gap renormalisation. Fig. S7–S10 (ESI†) further show the evolution of emission spectra at various pump intensities. All samples exhibited a trend similar to that of the thin perovskite microdisks, whereby the mode spacing decreased and the mode number increased with increasing diameter. Fig. 5b and Fig. S5 (ESI†) show that the mode spacing ($\Delta\lambda$) of all thick samples increases linearly with an increase in $1/D$, indicating consistent linear dependence; this finding demonstrated that all microdisks were well matched to the WGM. Moreover, we investigated the thickness-dependent lasing threshold. As shown in Fig. 5c, the lasing threshold increased with increasing the vertical thickness. Notably, the lowest lasing threshold of ~ 3 μJ cm^{-2} was observed in the 70 nm and 265 nm-thick microdisks.

To further investigate the cavity energy confinement effect, we introduced transient absorption (TA) to elucidate carrier dynamics. The typical TA spectra of the 265 nm perovskite films are shown in Fig. 6a. These TA spectra contained three main spectral features: photon-induced absorption (PA1 and PA2) and photon bleaching (PB), consistent with findings in the literature. From the time-resolved TA spectra, we could easily extract the carrier lifetimes of the perovskite films. Fig. 6b and Fig. S11 (ESI†) show the lifetimes of perovskite samples with various film thicknesses. Notably, the thickness of 265 nm exhibited the longest carrier lifetime. Carriers with longer lifetime indicated that the accumulation time of carrier density during the excitation process was extended. Concomitantly, carriers were available for population inversion and lasing action in the cavity, thus reducing the pumping threshold.

In recent years, perovskite WGM micro resonators have been identified as excellent candidates for construction of low-threshold and narrow-linewidth lasers. In this work, we produced high-performance $FAPbI_3$ perovskite microdisks lasers (with a threshold of ~ 3 μJ cm^{-2}) *via* fs laser direct writing. This threshold value is comparable to or better than the values for

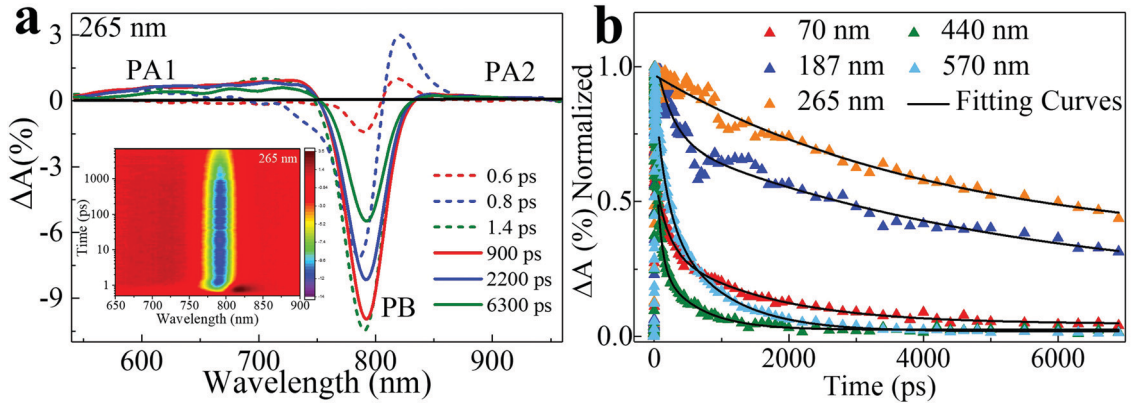

Fig. 6 (a) Time-resolved TA spectra (inset shows two-dimensional plot of typical transient absorption spectrum of perovskite films) and (b) comparison of carrier lifetime of perovskite films with various thicknesses.

Table 1 Comparison of organic–inorganic perovskite WGM lasing with different fabrication methods

Materials and microstructures	Fabrication methods	Pumping conditions	Threshold ($\mu J\ cm^{-2}$)	Year	Ref.
WGM lasing in perovskite microstructures					
$MAPbI_3$ (MPLs)	Vapor phase deposition	150 fs, 1 kHz (400 nm)	37	2014	43
$MAPbX_3$ (MDs)	One-step solution self-assembled	120 fs, 1 kHz (400 nm)	3.6	2015	42
$MAPbI_3$ (hexagonal MPs)	Growth technology with a buffer layer	50 fs, 1 kHz (400 nm)	11	2016	21
$MAPbBr_3$ (MPLs)	Lithography	100 fs, 1 kHz (400 nm)	2.3–3.4	2017	26
$MAPbBr_3$ (MDs)	Solution-based one-step anti-solvent		3.5	2018	44
$MAPbBr_3$ (triangular NPLs)	Vapor phase deposition	290 fs, 6 kHz (343 nm)	18.7	2019	45
$FAPbI_3$ (MDs)	Femtosecond laser direct writing	267 fs, 5 kHz (532 nm)	3	2020	Present work

various reported lasers based on organic–inorganic perovskite WGM lasing with different fabrication methods, as shown in Table 1. Our low threshold can be attributed to the following three factors: (1) evaporated $FAPbI_3$ films exhibit extremely minimal surface roughness and negligible light scattering; (2) fs laser fabrication demonstrates high spatial resolution and low surrounding damage, offering smooth edges and reproducible shapes; and (3) evaporated perovskite films are uniform and much thinner, compared with reported single crystal samples,[42] thereby offering better light confinement.

4. Conclusions

In summary, we have demonstrated low-threshold perovskite microdisk lasers by using a facile, top-down method (*i.e.*, fs laser direct writing). Perovskite microdisks were fabricated based on high-quality thermal co-evaporated $FAPbI_3$ films, which possess small grains, controllable thickness, and a smooth surface with reduced roughness. By using this highly reproducible and controllable fabrication method, we investigated the influence of microdisk dimensions (diameter and thickness) on laser performance. Importantly, we found that the lasing performance (*i.e.*, pump threshold, mode spacing, and mode numbers) was highly dependent on microdisk diameter, which is consistent with WGM theory and the findings in previous reports. However, microdisk thickness does not greatly affect the WGM; it can cause a slight shift of emission spectra and influence film quality (*i.e.*, improved carrier lifetime), as indicated by transient absorption measurements. After optimisation, a low threshold of $\sim 3\ \mu J\ cm^{-2}$ can be observed from these perovskite microdisks, which is non-trivial and suggests considerable potential for applications in next-generation nanophotonics.

Conflicts of interest

There are no conflicts to declare.

Acknowledgements

This work was financially supported by the Strategic Priority Research Program of the Chinese Academy of Sciences (Grant No. XDA25040102), the National Natural Science Foundation of China (Grant No. 51727901), the Natural Science Foundation of Hubei Province, China (Grant No. 2018CFA021 and 2019AAA020), the Fundamental Research Funds for the Central Universities (Grant No. 2042018kf0207 and 2042019kf0011), and the Wuhan Science and Technology Project of China (Grant No. 2019010701011420).

References

1 N. Zhang, Y. Fan, K. Wang, Z. Gu, Y. Wang, L. Ge, S. Xiao and Q. Song, *Nat. Commun.*, 2019, **10**, 1770.
2 H. Zhu, Y. Fu, F. Meng, X. Wu, Z. Gong, Q. Ding, M. V. Gustafsson, M. T. Trinh, S. Jin and X. Zhu, *Nat. Mater.*, 2015, **14**, 636–642.
3 Q. Zhang, R. Su, X. Liu, J. Xing, T. C. Sum and Q. Xiong, *Adv. Funct. Mater.*, 2016, **26**, 6238–6245.
4 N. Zhang, W. Sun, S. P. Rodrigues, K. Wang, Z. Gu, S. Wang, W. Cai, S. Xiao and Q. Song, *Nat. Mater.*, 2017, **29**, 1606205.
5 M. Li, Q. Wei, S. K. Muduli, N. Yantara, Q. Xu, N. Mathews, S. G. Mhaisalkar, G. Xing and T. C. Sum, *Adv. Mater.*, 2018, **30**, e1707235.
6 G. Xing, S. Sun, S. S. Lim, Y. M. Lam, M. Grätzel, S. Mhaisalkar and T. C. Sum, *Nature*, 2013, **342**, 344–347.
7 C. Wehrenfennig, G. E. Eperon, M.B. Johnston, H. J. Snaith and L. M. Herz, *Adv. Mater.*, 2014, **26**, 1584–1589.
8 F. Yuan, Z. Wu, H. Dong, B. Xia, J. Xi, S. Ning, L. Ma and X. Hou, *Appl. Phys. Lett.*, 2015, **107**, 261106.
9 Q. Dong, Y. Fang, Y. Shao, P. Mulligan, J. Qiu, L. Cao and J. Huang, *Science*, 2015, **347**, 967–970.
10 W. A. Dunlap-Shohl, Y. Zhou, N. P. Padture and D. B. Mitzi, *Chem. Rev.*, 2019, **119**, 3193–3295.
11 K. J. Vahala, *Nature*, 2003, **424**, 839–846.
12 P. J. Cegielski, A. L. Giesecke, S. Neutzner, C. Porschatis, M. Gandini, D. Schall, C. A. R. Perini, J. Bolten, S. Suckow, S. Kataria, B. Chmielak, T. Wahlbrink, A. Petrozza and M. C. Lemme, *Nano Lett.*, 2018, **18**, 6915–6923.
13 S. Wang, Y. Liu, G. Li, J. Zhang, N. Zhang, S. Xiao and Q. Song, *Adv. Opt. Mater.*, 2018, **6**, 1701266.
14 Q. Zeng, E. Lafalce, C. H. Lin, M. J. Smith, J. Jung, Y. Yoon, Z. Lin, V. V. Tsukruk and Z. V. Vardeny, *Nano Lett.*, 2019, **19**, 6049–6057.
15 S. McCall, A. Levi, R. Slusher, S. Pearton and R. Logan, *Appl. Phys. Lett.*, 1992, **60**, 289–291.
16 D. J. Gargas, M. C. Moore, A. Ni, S.-W. Chang, Z. Zhang, S.-L. Chuang and P. Yang, *ACS Nano*, 2010, **4**, 3270–3276.

17 R. Chen, B. Ling, X. W. Sun and H. D. Sun, *Adv. Mater.*, 2011, **23**, 2199–2204.
18 L. He, Ş. K. Özdemir and L. Yang, *Laser Photonics Rev.*, 2013, **7**, 60–82.
19 C. Raman and G. Sutherland, *Nature*, 1921, **108**, 42.
20 S. Yang, Y. Wang and H. Sun, *Adv. Opt. Mater.*, 2015, **3**, 1136–1162.
21 X. Liu, L. Niu, C. Wu, C. Cong, H. Wang, Q. Zeng, H. He, Q. Fu, W. Fu, T. Yu, C. Jin, Z. Liu and T. C. Sum, *Adv. Sci.*, 2016, **3**, 1600137.
22 J. Feng, X. Yan, Y. Zhang, X. Wang, Y. Wu, B. Su, H. Fu and L. Jiang, *Adv. Mater.*, 2016, **28**, 3732–3741.
23 G. Wang, D. Li, H.-C. Cheng, Y. Li, C.-Y. Chen, A. Yin, Z. Zhao, Z. Lin, H. Wu and Q. He, *Sci. Adv.*, 2015, **1**, e1500613.
24 M. S. Alias, Y. Yang, T. K. Ng, I. Dursun, D. Shi, M. I. Saidaminov, D. Priante, O. M. Bakr and B. S. Ooi, *J. Phys. Chem. Lett.*, 2016, **7**, 137–142.
25 J. Xing, X. F. Liu, Q. Zhang, S. T. Ha, Y. W. Yuan, C. Shen, T. C. Sum and Q. Xiong, *Nano Lett.*, 2015, **15**, 4571–4577.
26 N. Zhang, W. Sun, S. P. Rodrigues, K. Wang, Z. Gu, S. Wang, W. Cai, S. Xiao and Q. Song, *Adv. Mater.*, 2017, **29**, 1606205.
27 M. Hörantner, W. Zhang, M. Saliba, K. Wojciechowski and H. Snaith, *Energy Environ. Sci.*, 2015, **8**, 2041–2047.
28 Z. Song, S. C. Watthage, A. B. Phillips, B. L. Tompkins, R. J. Ellingson and M. J. Heben, *Chem. Mater.*, 2015, **27**, 4612–4619.
29 J. S. Manser, M. I. Saidaminov, J. A. Christians, O. M. Bakr and P. V. Kamat, *Acc. Chem. Res.*, 2016, **49**, 330–338.
30 N. Pourdavoud, S. Wang, A. Mayer, T. Hu, Y. Chen, A. Marianovich, W. Kowalsky, R. Heiderhoff, H.-C. Scheer and T. Riedl, *Adv. Mater.*, 2017, **29**, 1605003.
31 N. Pourdavoud, T. Haeger, A. Mayer, P. J. Cegielski, A. L. Giesecke, R. Heiderhoff, S. Olthof, S. Zaefferer and I. Shutsko, *Adv. Mater.*, 2019, **31**, e1903717.
32 N. Pourdavoud, A. Mayer, M. Buchmüller, B. Kai and T. R. Technologies, *Adv. Mater. Technol.*, 2018, **3**, 1700253.
33 G. E. Eperon, S. D. Stranks, C. Menelaou, M. B. Johnston, L. M. Herz and H. Snaith, *Energy Environ. Sci.*, 2014, **7**, 982–988.
34 W. S. Yang, J. H. Noh, N. J. Jeon, Y. C. Kim, S. Ryu, J. Seo and S. Il Seok, *Science*, 2015, **348**, 6240.
35 A. Binek, F. C. Hanusch, F. C. P. Docampo and T. Bein, *J. Phys. Chem. Lett.*, 2015, **6**, 1249–1253.
36 T. Liu, Y. Zong, Y. Zhou, M. Yang, Z. Li, O. S. Game, K. Zhu, R. Zhu, Q. Gong and N. P. Padture, *Chem. Mater.*, 2017, **29**, 3246–3250.
37 Y. Zhang, C.-K. Lim, Z. Dai, G. Yu, J. W. Haus, H. Zhang and P. N. Prasad, *Phys. Rep.*, 2019, **795**, 1–51.
38 R. F. Oulton, V. J. Sorger, T. Zentgraf, R.-M. Ma, C. Gladden, L. Dai, G. Bartal and X. Zhang, *Nature*, 2009, **461**, 629–632.
39 A. Reisinger, P. Zory and R. Waters, *IEEE J. Quantum Electron.*, 1987, **23**, 993–999.
40 F. Sasaki, M. Mori, S. Haraichi, Y. Ido, Y. Masumoto and S. Hotta, *Org. Electron.*, 2010, **11**, 1192–1198.
41 Q. Wei, X. Li, C. Liang, Z. Zhang, J. Guo, G. Hong, G. Xing and W. Huang, *Adv. Opt. Mater.*, 2019, **7**, 1900080.
42 Q. Liao, K. Hu, H. Zhang, X. Wang, J. Yao and H. Fu, *Adv. Mater.*, 2015, **27**, 3405–3410.
43 Q. Zhang, S. T. Ha, X. Liu, T. C. Sum and Q. Xiong, *Nano Lett.*, 2014, **14**, 5995–6001.
44 Z. Duan, Y. Wang, G. Li, S. Wang, N. Yi, S. Liu, S. Xiao and Q. Song, *Laser Photonics Rev.*, 2018, **12**, 1700234.
45 G. Li, T. Che, X. Ji, S. Liu, Y. Hao, Y. Cui and S. Liu, *Adv. Funct. Mater.*, 2019, **29**, 1805553.

